Temporally resolved single cell transcriptomics in a human model of amniogenesis

AUTHORS: Nikola Sekulovski[1,¶], Amber E. Carleton[1,¶], Anusha A. Rengarajan[1,¶], Chien-Wei Lin[2,¶], Lauren N. Juga[1], Allison E. Whorton[1], Jenna K. Schmidt[3], Thaddeus G. Golos[3,4,5], and Kenichiro Taniguchi[1,6,7,†]

AFFILIATIONS:

[1]Department of Cell Biology, Neurobiology and Anatomy, Medical College of Wisconsin, Milwaukee, WI 53226, USA

[2]Division of Biostatistics, Institute for Health and Equity, Medical College of Wisconsin, Milwaukee, WI 53226, USA

[3]Wisconsin National Primate Research Center (WNPRC), Madison, WI, USA

[4]Department of Obstetrics and Gynecology, University of Wisconsin - Madison School of Medicine, Madison, WI USA

[5]Department of Comparative Biosciences, University of Wisconsin - Madison School of Veterinary Medicine, Madison, WI, USA

[6]Department of Pediatrics, Medical College of Wisconsin, Milwaukee, WI 53226, USA

[7]Cancer Center, Medical College of Wisconsin, Milwaukee, WI 53226, USA

[¶]These authors contributed equally to this work

[†]Corresponding author

CONTACT:

Kenichiro Taniguchi

8701 Watertown Plank Road

B4245 BSB CB062

Milwaukee, WI 53226

ktaniguchi@mcw.edu

ABSTRACT

Amniogenesis is triggered in a collection of pluripotent epiblast cells as the human embryo implants. To gain insights into the critical but poorly understood transcriptional machinery governing amnion fate determination, we examined the evolving transcriptome of a developing human pluripotent stem cell-derived amnion model at the single cell level. This analysis revealed five continuous amniotic fate progressing states with state-specific markers, which include a previously unrecognized CLDN10^{+} amnion progenitor state. Strikingly, we found that expression of CLDN10 is restricted to the amnion-epiblast boundary region in the human post-implantation amniotic sac model as well as in a peri-gastrula cynomolgus macaque embryo, bolstering the growing notion that, at this stage, the amnion-epiblast boundary is a site of active amniogenesis. Bioinformatic analysis of published primate peri-gastrula single cell sequencing data further confirmed that CLDN10 is expressed in cells progressing to amnion. Additionally, our loss of function analysis shows that CLDN10 promotes amniotic but suppresses primordial germ cell-like fate. Overall, this study presents a comprehensive amniogenic single cell transcriptomic resource and identifies a previously unrecognized CLDN10^{+} amnion progenitor population at the amnion-epiblast boundary of the primate peri-gastrula.

INTRODUCTION

Amniogenesis is initiated during implantation in humans, and leads to the formation of an amniotic sac structure that surrounds and protects the developing embryo (Enders et al., 1983; Enders et al., 1986; Miki et al., 2005; Sasaki et al., 2016; Shahbazi and Zernicka-Goetz, 2018; Taniguchi et al., 2019). At implantation, the embryo (referred to at this time as a blastocyst) contains three morphologically and molecularly distinct cell types: 1) a collection of unpolarized pluripotent epiblast cells, precursors to both the embryo proper and the amniotic ectoderm, 2) a surrounding layer of polarized trophectoderm, a placental tissue precursor, and 3) an underlying extraembryonic primitive endoderm, a yolk sac precursor. Upon implantation, the pluripotent epiblast cells initiate epithelial polarization to form a cyst with a central lumen, the future amniotic cavity (Carleton et al., 2022; Shao and Fu, 2022). This event is followed by the fate transition of pluripotent epiblast cells that are in close proximity to the uterus to squamous amniotic ectoderm, forming a clear boundary between amnion and pluripotent epiblast territories of the cyst (Shahbazi and Zernicka-Goetz, 2018; Shao and Fu, 2022; Taniguchi et al., 2019). This asymmetric amnion-epiblast structure, known as the amniotic sac, provides the foundation for the next essential developmental steps (e.g., primitive streak formation, neural specification).

Recent studies using early human and monkey embryos have provided a basic understanding of the transcriptomic characteristics of early primate amniogenesis (Bergmann et al., 2022; Nakamura et al., 2016; Nakamura et al., 2017; Sasaki et al., 2016; Tyser et al., 2021; Yang et al., 2021). Yet, experimental dissection of the molecular mechanisms involved in this process is difficult in these *in vivo* models. To

enable molecular and cellular investigations, we and others developed human pluripotent stem cell (hPSC)-derived amnion models and showed that BMP signaling plays a crucial role in initiating amniogenesis (Chen et al., 2021; Overeem et al., 2023; Shao et al., 2017a; Shao et al., 2017b; Zheng et al., 2019). Recently, we further explored the BMP-dependent amniogenic transcriptional cascade, identifying several distinct transcriptional stages, as well as a requirement for TFAP2A-dependent transcription in regulating amnion fate progression (Sekulovski et al., 2023). However, changes in cellular differentiation states during amnion lineage progression remain largely unexplored.

In this study, we used single cell RNA sequencing (scRNA-seq) analysis to examine the dynamics in gene expression that accompany amnion differentiation of hPSC (herein referred to as the hPSC-amnion) cultured in a soft gel environment, called Gel-3D (Shao et al., 2017a). While no exogenous BMP is added in this Gel-3D amnion model, BMP signaling is activated in the cells by a mechanosensitive cue provided by the soft substrate, thereby initiating human amniogenesis (Shao and Fu, 2022; Shao et al., 2017a; Taniguchi et al., 2019). Interestingly, our data reveal five contiguous amniogenic cell states: pluripotency-exiting, early progenitor, late progenitor, specified and maturing, each of which shows transcriptional similarities to distinct cell types in a Carnegie stage 7 human embryo (Tyser et al., 2021). Our data also reveal the presence of two non-amniotic cell types in the Gel-3D system: primordial germ cell-like and cardiac mesoderm-like cells. Importantly, we identify a cohort of markers specific to each of these five amnion lineage progressing states, and validate selected markers for their expression in the amnion from cynomolgus macaque (*Macaca fascicularis*)

embryos. Strikingly, we show that CLDN10, a marker of the progenitor population, exhibits a restricted amniotic expression pattern at the boundary between the amnion and the epiblast of the cynomolgus macaque peri-gastrula. This further supports our findings from a separate study (Sekulovski et al., 2023), which show that the amnion-epiblast boundary is a site of active amniogenesis in the macaque peri-gastrula. Furthermore, loss of CLDN10 results in the formation of primordial germ cell-like cells at the expense of amnion cells. Together, this study provides important single cell-level insight into human amnion fate progression and presents additional evidence for the presence of amnion progenitor cells in primate embryos undergoing gastrulation.

RESULTS

Previously, we described culture conditions (Gel-3D) in which plated hPSC form polarized cysts initially composed of columnar pluripotent cells, which then spontaneously undergo squamous morphogenesis and begin to express amnion markers (Shao et al., 2017a). Specifically, singly dissociated hPSC are plated densely on a soft gel substrate to form aggregates and are allowed to grow for 24 hours (hrs) in the presence of a ROCK inhibitor (Y-27632). After the first 24 hrs (day 1, d1), the ROCK inhibitor is removed (a trigger to initiate lumenal cyst formation (Hamed et al., 2023; Shao et al., 2017a; Taniguchi et al., 2015)), and a diluted extracellular matrix gel overlay (2% v/v, e.g., Geltrex) is added to provide an additional 3D cue. Immunofluorescent (IF) staining at this time shows cuboidal cells surrounding a central lumen; these cells express NANOG, but not TFAP2A (**Fig. 1A**).

116 Interestingly, 24 hrs after adding the gel overlay (d2), a subset of cells within the
117 cysts displays reduced expression of NANOG, while TFAP2A expression becomes
118 weakly activated (**Fig. 1A**, arrowhead in d2). By d3, NANOG is no longer detectable.
119 Moreover, while many cells exhibit prominent TFAP2A expression, some cells are only
120 weakly positive for TFAP2A (**Fig. 1A**, arrowheads). This pattern of TFAP2A expression
121 is consistent with the previous observation that amniogenesis initiates focally on the
122 pluripotent cysts and then spreads laterally to form fully squamous cysts (**Fig. 1A**,
123 (Sekulovski et al., 2023; Shao et al., 2017a; Shao et al., 2017b)). These molecular
124 changes are accompanied by a decrease in nuclear aspect ratio (a measure of
125 epithelial cell morphology) over time, revealing more flattened (squamous) shapes by
126 d3 and d4 (**Fig. 1B**, quantitation strategy shown in **Fig. S1A**, and previously established
127 in Shao et al., 2017a; Townshend et al., 2020)). These results provide further molecular
128 and structural evidence that the transition from pluripotent to amnion cell types occurs
129 progressively over the cyst, starting from focal initiation sites (Sekulovski et al., 2023;
130 Shao et al., 2017a; Shao et al., 2017b).
131 To explore transcriptional programs of the fate transitioning cells during early
132 stages of human amnion development in this model, we performed time-course scRNA-
133 seq analysis of developing hPSC-amnion cysts, harvested at d1, d2, d3 and d4. hPSC-
134 amnion cysts were dissociated into single cells, followed by single cell isolation and
135 labeling using the 10x Genomics Chromium system, cDNA amplification and
136 sequencing followed by demultiplexing (see Material and Methods for additional details).
137 This scRNA-seq dataset was examined using Seurat (Butler et al., 2018) for data
138 filtering, regression for genes associated with cell cycle progression, normalization,

139 variable gene selection and subsequent unsupervised clustering of cells (see Materials
140 and Methods). The data yield seven distinct populations among 8,765 cells (d1 = 1,359
141 (salmon), d2 = 1,546 (sage), d3 = 2,352 (light blue), d4 = 3,508 cells (purple), **Fig. 1C**),
142 which, after marker and lineage analyses described below, are labeled pluripotency-
143 exiting (salmon color, 1,363 cells), early progenitor (brown, 479 cells), late progenitor
144 (sage, 1,045 cells), specified (green, 1,366 cells) and maturing (purple, 2,795 cells),
145 PGC-LC (primordial germ cell-like cells, blue, 1,055 cells) and CM-LC (cardiac
146 mesoderm-like cells, magenta, 662, **Fig. 1D**). Transcriptomic features of these cells are
147 visualized in Uniform Manifold Approximation and Projection (UMAP) plots (**Fig. 1C,D**).
148 To broadly characterize the transcriptional state of each population, we examined
149 the expression of known amnion markers (Roost et al., 2015; Shao et al., 2017a; Yang
150 et al., 2021; Zhao et al., 2024; Zheng et al., 2022). Consistent with the amniotic lineage,
151 early amnion markers (*ID2*, *GATA3* and *TFAP2A*, **Fig. 1E**, expression superimposed on
152 the UMAP plot in **Fig. 1C**) are widely expressed starting at d1 in pluripotency-exiting
153 cells that also show broad expression of pluripotency markers (**Fig. S1B**), while
154 intermediate markers that label specified amnion (*ISL1*, *HAND1*, *DLX5*, (Sekulovski et
155 al., 2023; Yang et al., 2021; Zhao et al., 2024)) show abundant expression by d3 (**Fig.
156 1F**). Late amnion genes such as *GABRP*, *VTCN*1 and *IGFBP3* (expressed in the first-
157 trimester human amnion (Roost et al., 2015) and also in other human amnion models
158 (Sekulovski et al., 2023; Shao et al., 2017a; Yang et al., 2021; Zhao et al., 2024; Zheng
159 et al., 2022)) are primarily enriched in the d3 and d4 populations (**Fig. 1G**). Interestingly,
160 most of the d2 cells show the expression of early, but not specified or pluripotency
161 (SOX2, NANOG), genes, suggesting that the d2 cell population may contain

162 transitioning cell types that give rise to specified amnion (brown and sage cells in **Fig.**
163 **1D**). Next, RNA-velocity analysis (Bergen et al., 2020) was applied to examine lineage
164 relationships based on the relative abundance of unspliced and spliced mRNA in each
165 cell. Indeed, the majority of the RNA-vector trajectories are directed from the cells in the
166 early progenitor (brown), late progenitor (sage), to specified (green) states (**Fig. 1H**).
167 In a recent study, we performed a detailed meta-analysis of the Tyser *et al.*
168 scRNA-seq dataset from a human embryo staged at Carnegie stage 7 (CS7) (Tyser et
169 al., 2021) and showed that the rod-shaped cluster of cells annotated as "Ectoderm" is
170 comprised of lineage progressing, lineage committed, and fully differentiated amnion
171 cell types (Sekulovski et al., 2023). The Tyser *et al*. UMAP plot is reproduced in **Fig.**
172 **S1C** with the original coordinates and annotations (expression of late markers, *GABRP*,
173 *VTCN*1 and *IGFBP3*, found at the distal tip of the rod-shaped "Ectoderm" population,
174 **Fig. S1C-E**). To examine which cells in the CS7 human embryo share transcriptomic
175 similarities to amnion progressing cells in Gel-3D, the scRNA-seq datasets from the
176 Tyser *et al.* CS7 human embryo and our d1-d4 Gel-3D time-course samples were
177 combined and normalized using an integration feature based on canonical correlation
178 analysis in Seurat (Hao et al., 2021) (**Fig. 1I-K**). Although the combined UMAP plot of
179 this integrated dataset shows some changes in shape from our original UMAP, it is clear
180 that "Epiblast", "Primitive Streak" and "Ectoderm" populations in the Tyser *et al.* dataset
181 closely map to the amnion progressing populations in our time-course Gel-3D dataset
182 (**Fig. 1I**, see **Fig. S1F** for mapping of each population). Indeed, the amniotic Tyser
183 "Ectoderm" cells primarily overlap with Gel-3D "specified" and "maturing" cell
184 populations, consistent with their amniotic fate; most Tyser "Epiblast" cells are seen in

185 the “pluripotency-exiting” population (**Fig. 1J,K**, **Fig. S1F**). Interestingly, Tyser “Primitive
186 Streak” cells are populated across several Gel-3D amniogenic cell states (**Fig. 1J,K**,
187 **Fig. S1F**), overlapping with the early (brown) and late (sage) progenitor populations,
188 suggesting that some Tyser “Primitive Streak” cells may be actively transitioning, and
189 that our early and late progenitor cells may display transcriptomic characteristics of fate
190 transitioning cells in human peri-gastrula.

191 Additionally, we identify two non-amniotic cell types that show transcriptional
192 characteristics of PGC- (blue) and CM- (magenta) like cells (**Fig. 1D**). The Tyser-Gel-3D
193 integration analysis shows that the blue cells overlap with the Tyser “Primitive Streak”
194 cells that abundantly express PGC markers (e.g., *PRDM1*, *SOX17*, *NANOS3*, *PRDM14*,
195 *NANOG*, *XACT*, **Fig. 1L**). Several Tyser “Advanced Mesoderm” cells are seen in the
196 magenta cells, and our marker analysis shows that cardiac mesoderm makers (*HAND2*,
197 *GATA4*, *PITX2*, *ISL1*, *HAND1*) are enriched, indicating their cardiac lineage (**Fig. 1M**,
198 summary of additional markers found in **Fig. 1N**). Strikingly, the RNA velocity
199 trajectories are directed from the interface of the early/late amnion progenitor
200 populations to the PGC-LC (**Fig. 1H**), suggesting their close transcriptomic
201 characteristics. These findings support a growing notion that amnion and PGC
202 progressing cells initially share a common intermediate lineage (Castillo-Venzor et al.,
203 2023; Chen et al., 2019; Zheng et al., 2022). The CM-LC population may have formed
204 due to high BMP signaling (Schultheiss et al., 1997; Tsaytler et al., 2023; van Wijk et al.,
205 2007).

206 To identify genes that are unique to each cluster, unsupervised differential gene
207 enrichment analysis was performed (**Table 1**, adjusted p-value < 0.05). As expected,

208 pluripotency markers are seen in the pluripotency-exiting cluster, and the specified and
209 maturing clusters show enriched expression of known late amnion markers as well as
210 previously uncharacterized genes (*ADAMTS18*, *SESN3* (**Fig. 1N**) – RNA *in situ*
211 hybridization in a cynomolgus macaque (*Macaca fascicularis*) embryo staged between
212 CS12 and CS13, an organogenesis stage, shown in **Fig. S2A-C**).

213 The most differentially expressed genes in early (brown) and late (sage)
214 progenitor populations are *TBXT* (T-box transcription factor T) and *CLDN10* (a gene
215 encoding Claudin-10, a component of the tight junction), respectively (**Fig. 2A,B**, top
216 three genes plotted in **Fig. 2C**). Recently, we showed that amnion lineage progression
217 in Glass-3D^{+BMP}, another model of human amniogenesis, traverses an intermediate
218 transcriptional phase weakly expressing *TBXT* (*TBXT*^{low}) before specified markers (e.g.,
219 *ISL1*, *HAND1*, *DLX5*) are expressed, revealing lineage progressing characteristics of
220 the cells in the *TBXT*^{low} transcriptional phase (Sekulovski et al., 2023). The same study
221 also showed that cells displaying transcriptomic characteristics consistent with fate
222 progression from *TBXT*^{low} to *ISL1*$^{+}$/*HAND1*$^{+}$ specified state are also seen in the Tyser *et*
223 *al.* CS7 human embryo as well in the Yang *et al.* d14 cynomolgus macaque embryo
224 datasets (Sekulovski et al., 2023). In Gel-3D, while most cells in the early progenitor
225 population express some level of *TBXT*, only a few cells express abundant *TBXT* (**Fig.**
226 **2A**). Indeed, our IF time-course analysis shows that cells with weak TBXT expression
227 are seen at d2 in several cells that are not yet expressing ISL1 (**Fig. 2D**, arrowheads);
228 TBXT expression is largely missing in d3 and d4 cysts (**Fig. 2D**), confirming the
229 presence of an early and transient *TBXT*^{low} state in developing Gel-3D hPSC-amnion
230 cysts.

231 Prominent *CLDN10* expression is seen throughout the late progenitor population
232 (*CLDN10*^{high}), but is rapidly diminished in the specified cells (**Fig. 2B**). Although at lower
233 levels, some *CLDN10* expression is observed in the pluripotency-exiting and early
234 progenitor states (*CLDN10*^{low}, **Fig. 2B,C**), consistent with our previous bulk-RNA
235 sequencing analysis showing that low *CLDN10* expression is seen in pluripotent cells
236 (Shao et al., 2017a). Using IF staining in Gel-3D hPSC-amnion model, we validated a
237 dynamic expression pattern of CLDN10 over time (**Fig. 2D,E**). Despite broadly
238 expressed at transcript levels in hPSC-amnion cysts at d2 (**Fig. 2B**), CLDN10
239 expression is seen in the small fraction of cells that are weakly positive for TBXT and
240 TFAP2A (**Fig. 2D,E**, arrowheads, quantitation in **Fig. 2F**). At d3, CLDN10 is co-
241 expressed with TFAP2A in several, but not all cells (**Fig. 2E**). Further, ISL1^{high} cells do
242 not show clear CLDN10 membrane staining (**Fig. 2D**). In contrast, most cells at d4
243 retain abundant TFAP2A and ISL1 expression but do not express CLDN10 (**Fig. 2D,E**).
244 Importantly, our analysis for nuclear aspect ratio (NAR) shows that, at d2, CLDN10^{+}
245 cells (mean NAR = 0.54 $\pm$ 0.17 STDEV, n = 39) are significantly more squamous
246 compared to CLDN10^{-} cells (NAR = 0.97 $\pm$ 0.31 STDEV, n = 87, $p<0.001$). While
247 previous studies implicated *CLDN10* as an amnion marker (Zheng et al., 2019; Zheng et
248 al., 2022), a detailed analysis was not performed. Thus, these data present evidence
249 suggesting that CLDN10^{high} marks a later transient progenitor state that follows an
250 earlier *TBXT*^{low}/*CLDN10*^{low} progenitor state, but CLDN10 expression is extinguished in
251 more differentiated cells. Single cell transcriptomic characteristics consistent with this
252 lineage progression from the *TBXT*^{low}/*CLDN10*^{low} state to the *CLDN10*^{high} state is also

253 seen in the Tyser *et al.* CS7 human embryo as well in the Yang *et al.* d14 cynomolgus
254 macaque embryo datasets (**Fig. S3A-C**).
255 Interestingly, in PASE (post-implantation amniotic sac embryoids), an *in vitro*
256 model of human amniotic sac formation (Shao et al., 2017b), CLDN10 is localized
257 specifically to cells at the boundary between squamous amnion and columnar
258 pluripotent cells (**Fig. 3A** , arrowheads). To test whether CLDN10^{+} progenitor-like
259 boundary cells are present in the developing primate amniotic sac *in vivo*, we analyzed
260 CLDN10 expression in a cynomolgus macaque embryo displaying the amniotic sac
261 (**Fig. 3B**, staged between CS6 and CS7). Strikingly, CLDN10 expression is exclusively
262 seen at the boundary separating amnion and epiblast tissues. These results are
263 consistent with our recent findings indicating that this boundary is likely a site of active
264 amniogenesis (i.e., epiblast cells at the boundary actively undergo amnion specification)
265 in the primate peri-gastrula (Sekulovski et al., 2023). Importantly, a cynomolgus
266 macaque embryo from a later stage (**Fig. 3C,D**, CS10) also shows CLDN10 positive
267 cells at the amnion-embryo boundary. In the CS10 embryo, while a collection of cells
268 expressing weak CLDN10 is seen posteriorly (**Fig. 3C,D** – inset (iii)), CLDN10
269 expression is highly prominent anteriorly in the cells at the boundary of the amnion and
270 the developing mediolateral placode (**Fig. 3C,D** – inset (i), additional images in **Fig.**
271 **S3D,E**). Together, these results establish the presence of previously unrecognized
272 CLDN10^{+} amnion-embryo boundary population that primarily gives rise to amnion
273 during gastrulation as well as during early organogenesis in the cynomolgus macaque.
274 To investigate the role of CLDN10, H9 hESC lacking CLDN10 were cultured in
275 the Gel-3D condition (**Fig. 4A-D**, see **Fig. S4** for generation of *CLDN10*-KO lines).

276 Morphologically, while *CLDN10*-KO cyst formation is largely similar to controls by d3, by
277 d4, squamous morphogenesis as well as overall cyst formation are disrupted.
278 Interestingly, our IF analysis shows that, in the KO background, SOX2 expression
279 gradually reduces overtime similar to controls, but cells expressing ISL1 are reduced by
280 d4 (**Fig. 4A,B**). Given the presence of PGC-LC in Gel-3D (**Fig. 1D,L**), we next
281 examined the expression of PGC markers. Strikingly, while very few cells are
282 $NANOG^{+}/SOX17^{+}$ PGC-LC in controls at d4, NANOG/SOX17 double positive cells are
283 seen prematurely at d2 as well as at d3 (**Fig. 4C,D**). These results suggest that
284 CLDN10 functions to promote amnion fate progression, and prevent emergence of the
285 PGC-like lineage.
286
287 **DISCUSSION**
288 Together, this study presents a temporally resolved single cell transcriptomic resource
289 for future investigations of the amniogenic transcriptional cascade in developing primate
290 embryos. In summary, we have profiled the transcriptomic signatures of lineage
291 progressing cells in an *in vitro* model of hPSC-amnion development, and identified 1)
292 five contiguous amnion progressing states (outlined in **Fig. 4E**) including two previously
293 unrecognized amnion progenitor populations, 2) an amnion progenitor population
294 labeled by CLDN10 at the boundary between the amnion and the epiblast of the primate
295 amniotic sac (model schematic in **Fig. 4F**), and 3) the role of CLDN10 in maintaining
296 amnion fate progression.
297 Our time-course scRNA-seq analysis showed that PGC-LC are present in our
298 Gel-3D model, and that some of the amnion progenitor population may contribute to

299 PGC-LC, supporting a growing notion that amnion and PGC progressing cells initially
300 share a common lineage (Castillo-Venzor et al., 2023; Chen et al., 2019; Xiao et al.,
301 2024; Zheng et al., 2022), and providing detailed transcriptomic insights into this lineage
302 diversification step that occurs in the Gel-3D system (**Fig. 4E**). Moreover, the loss of
303 CLDN10, a marker of the late amnion progenitor and a tight junction component, leads
304 to increased PGC-LC formation, while amnion formation is reduced. Interestingly, a
305 recent study by Vasic *et al.* showed that reduced level of TJP1 (also known as ZO-1) in
306 unconfined hPSC monolayer colonies treated with BMP4 (a system that undergoes
307 gastrulation-like patterning (Joy et al., 2021) similar to the micropatterned gastruloid
308 model, (Heemskerk et al., 2017; Warmflash et al., 2014) leads to increased emergence
309 of a germ cell lineage (Vasic et al., 2023). Therefore, our results present additional
310 evidence for the role of tight junction formation in suppressing PGC lineages, and
311 demonstrate a key role of CLDN10 in maintaining amnion fate progression in progenitor
312 cells. Given that Claudin proteins control tight junction properties and epithelial
313 characteristics (Angelow et al., 2008), CLDN10 might also be critical for organizing a
314 boundary structure containing shape/fate-transitioning cells flanked by squamous
315 amnion or columnar/pseudostratified pluripotent cells on each side.
316 Previous studies established that BMP is a major trigger of amniogenesis. What
317 other potential mechanisms could help to initially induce and maintain the half amnion-
318 half epiblast structure? Trophectoderm may play some roles in triggering amnion
319 specification given that these cells directly overlay the nascent amnion during
320 implantation. Indeed, molecular characterization of early cynomolgus macaque embryos
321 by Sasaki *et al.* (Sasaki et al., 2016) have suggested that the trophectoderm may

322 provide some cue (e.g., secreted ligands) to the underlying epiblast cells. Also, a recent
323 study by Pedroza *et al.* showed that co-culturing hPSC on a monolayer of human
324 trophoblast stem cells helps initiate amniogenesis (Pedroza et al., 2023).
325 Furthermore, visceral endoderm might play an important role in defining the zone
326 in which amniogenesis can occur, helping to shape the amnion-epiblast boundary
327 territory. Studies have established that visceral endoderm plays a major role in embryo
328 patterning by expressing secreted BMP antagonists (Chambers et al., 2009; Perea-
329 Gomez et al., 2002; Shawlot et al., 1999), even at very early stages of implantation
330 (Bergmann et al., 2022; Sasaki et al., 2016). Therefore, it is possible that, during
331 implantation, epiblast cells that are in close proximity to visceral endoderm contribute to
332 embryo proper because the presence of secreted BMP antagonists prevents them from
333 undergoing amniogenesis. However, more distal epiblast cells at the uterine-proximal
334 pole of the epiblast cyst, which are farther away from the BMP antagonist source, can
335 respond to BMP signaling and form amnion. The amnion-epiblast boundary territory
336 might be the most distal region at which amniogenesis can take place, and the balance
337 between the rate of epiblast proliferation and the rate of amniogenesis at the boundary
338 likely contributes to maintaining the ratio between amnion and epiblast cells in
339 implanting embryos, as well as in peri-gastrula.
340 Recently, single cell transcriptomics analysis has emerged as a valuable tool to
341 ground findings from *in vitro* models with natural as well as cultured primate embryo
342 systems (e.g., (Yang et al., 2021; Zhao et al., 2024; Zheng et al., 2022)). To aid in
343 additional investigations, several culture systems have been developed to generate
344 amnion, and single cell transcriptomic analyses have been performed in several of the

345 systems (e.g., (Chen et al., 2019; Minn et al., 2020; Overeem et al., 2023; Rostovskaya
346 et al., 2022)). Future transcriptomic comparisons of the amnion in each of these models
347 will enable us to gain additional insights into amniogenic mechanisms.
348

349 **MATERIALS AND METHODS**

350 *hESC lines*

351 Human embryonic stem cell line H9 was used in this study (WA09, P30, P48, WiCell;
352 NIH registration number: 0062). All protocols for the use of hPSC lines were approved
353 by the Human Stem Cell Research Oversight Committee at the Medical College of
354 Wisconsin and the Human Pluripotent Stem Cell Research Oversight Committee at the
355 University of Michigan. All hPSC lines were maintained in a feeder-free system for at
356 least 20 passages and authenticated as karyotypically normal at the indicated passage
357 number. Karyotype analysis was performed at Cell Line Genetics. All hPSC lines tested
358 negative for mycoplasma contamination (LookOut Mycoplasma PCR Detection Kit,
359 Sigma-Aldrich). In summary, hESC were maintained in a feeder-free culture system with
360 mTeSR1 medium, or with 50%/50% mix of mTeSR1 and mTeSR plus (STEMCELL
361 Technologies). hESC were cultured on 1% (v/v) Geltrex (Thermo Fisher Scientific), or
362 with Cultrex SCQ (Bio-techne) coated 6 well plates (Nunc). Cells were passaged as
363 small clumps every 4 to 5 days with Dispase (Gibco). All cells were cultured at 37°C
364 with 5% CO_2. Media was changed every day. hESC were visually checked every day to
365 ensure the absence of spontaneously differentiated, mesenchyme-like cells in the
366 culture. Minor differentiated cells were scratched off the plate under a dissecting scope
367 once identified. The quality of all hESC lines was periodically examined by

368 immunostaining for pluripotency markers and successful differentiation to three germ
369 layer cells. Similar methods were previously used in (Sekulovski et al., 2023; Wang et
370 al., 2021).
371
372 *Gel-3D hPSC-amnion formation assays*
373 Methods for these assays have been previously described (Shao et al., 2017a; Shao et
374 al., 2017b) with exceptions that 60-70uL of undiluted ECM gel solution is hand-streaked
375 on ice cold 22mmx22mm square coverslips, and that, in addition to Geltrex (Life
376 Technologies), Cultrex Ultimatrix (Bio-Techne) was also used. Singly dissociated cells
377 were prepared using Accutase (Sigma-Aldrich) and were plated on ECM gel-coated
378 coverslips at 25,000 cells/cm^2 in mTeSR1 or in 50%/50% mTeSR1/mTeSR plus mix
379 medium in the presence of 10μM Y-27632 (STEMCELL Technologies). After 24 hr, cells
380 were then incubated in media containing 2% Geltrex/Ultimatrix overlay without Y-27632
381 with daily media changes (note that 1% gel overlay was used between d2 to d4).
382
383 *DNA constructs*
384 *piggyBac-CRISPR/Cas9 (pBACON) constructs*
385 A piggyBac-CRISPR/Cas9 (pBACON) vector that contains SpCas9-T2A-puro and hU6-
386 gRNA expression cassettes flanked by piggyBac transposon terminal repeat elements
387 (pBACON-puro), which allows subcloning of annealed oligos containing gRNA
388 sequence at *BbsI* site, has been previously described (Shao et al., 2017b; Townshend
389 et al., 2020; Wang et al., 2021). gRNA targeting genomic sites and oligo sequences to
390 generate pBACON-puro-h*CLDN10*-ICL1 (primers: CRISPR_hCLDN10ICL#1_s and

391 CRISPR_hCLDN10ICL#1_as) are found in **Fig. S4** and **Table 2**; these were designed
392 using a publicly available tool
393 (https://www.idtdna.com/site/order/designtool/index/CRISPR_CUSTOM). Similar
394 methods were previously used in several publications (e.g., (Sekulovski et al., 2023;
395 Wang et al., 2021)).
396
397 *piggyBac-based transgenic and genome edited hESC lines*
398 PB constructs (3μg) and pCAG-ePBase (Lacoste et al., 2009) (1μg) were co-transfected
399 into H9 hESC (70,000 cells cm^{-2}) using GeneJammer transfection reagent (Agilent
400 Technologies). To enrich for successfully transfected cells, drug selection (puromycin,
401 2μg/mL for 4 days) was performed 48- to 72-hrs after transfection. hESC stably
402 expressing each construct maintained the expression of pluripotency markers.
403 During pBACON-based genome editing, puro-selected cells were cultured at low
404 density (300 cells cm^{-2}) for clonal selection. Established colonies were manually picked
405 and expanded for screening indel mutations using PCR amplification of a region
406 spanning the targeted gRNA region (genomic DNA isolated using DirectPCR Lysis
407 Reagent (Tail) (VIAGEN), primers: hCLDN10, Geno_hCLDN10CDS2_RI_fw and
408 Geno_hCLDN10CDS2_NI_rv), which were subcloned into pPBCAG-GFP (Chen and
409 LoTurco, 2012) at EcoRI and NotI sites, and sequenced (Seq-3'TR-pPB-Fw). At least
410 12 to 15 bacterial colonies were sequenced (Sanger sequencing) to confirm genotypic
411 clonality. Control cells are wild-type, unedited H9 hESC in all loss-of-function
412 experiments.
413

414 *Cynomolgus macaque*

415 *Animals*

416 The female and male cynomolgus macaques were housed and cared for at the Wisconsin
417 National Primate Research Center (WNPRC). All procedures were performed in
418 accordance with the NIH Guide for the Care and Use of Laboratory Animals and under
419 approval of the University of Wisconsin College of Letters and Sciences and Vice
420 Chancellor Office for Research and Graduate Education Institutional Animal Care and
421 Use Committee (protocol g005061).

422

423 *Animal breeding and pregnancy detection*

424 Beginning on day 8 post-onset of menses, the female was housed with a compatible
425 male and monitored for breeding. Animals were pair-housed until day 16-20 post-onset
426 of menses. A 2-3 mL blood draw was performed daily from day 8 post-onset of menses
427 until day 16 to assess the timing of ovulation based on the estradiol peak and rise in
428 progesterone in serum. Serum samples were analyzed for estradiol (25 μL) and
429 progesterone (20 μL) using a cobas e411 analyzer equipped with
430 ElectroChemiLuminescence technology (Roche, Basal, Switzerland) according to
431 manufacturer instructions. Results were determined via a calibration curve which was
432 instrument-generated by 2-point calibration using traceable standards and a master
433 curve provided via the reagent barcode. Inter-assay coefficient of variation (CV) was
434 determined by assaying aliquots of a pool of rhesus plasma. For estradiol, the limit of
435 quantitation (LOQ) was 25 pg/mL, the intra-assay CV was 2.02%, and the inter-assay
436 CV was 5.05%. For progesterone, the LOQ was 0.2 ng/mL, the intra-assay CV was

437 1.37%, and the inter-assay CV was 4.63%. A transabdominal ultrasound was performed
438 to detect pregnancy as early as 14 days post-ovulation. The ultrasound measurements
439 in combination with the timing of ovulation were used to estimate the day of conception
440 and gestational age of the pregnancy.
441
442 *Terminal perfusion uterine collection, paraffin embedding, sectioning and staining*
443 The pregnant females were sedated with intramuscular ketamine (>15 mg/kg) followed
444 by IV sodium pentobarbital (>35 mg/kg) and then perfused with 4% paraformaldehyde
445 (PFA) via the left ventricle. The entire uterus and cervix were removed. The serosa and
446 superficial myometrium were scored for better fixative penetration and to denote dorsal
447 and ventral orientation. Tissues were fixed in 4% PFA with constant stirring and solution
448 changes were performed every 24 hrs for a total of 72 hrs. The uterus was serially
449 sectioned from the fundus to the internal cervical os into 4 mm slices using a dissection
450 box. Cassettes with tissue sections were transferred into 70% ethanol, routinely
451 processed in an automated tissue processor and embedded in paraffin for histological
452 analyses (5 μm sections). Fixed uterine tissue were cut in 5 μm thick cross-sections,
453 mounted on slides, deparaffinized in xylene and rehydrated in an ethanol series. Antigen
454 retrieval was performed by boiling in citrate buffer. Sections were blocked 4% goat serum
455 in PBS at RT for at least 3-hr. Subsequent immunolocalization was performed using
456 commercially available primary antibodies, incubated overnight at 4 °C in 4% serum.
457 Immunofluorescent detection was performed using secondary antibodies tagged with a
458 fluorescent dye (fluorophores excitation = 488, 555, and 647nm), and counterstained with
459 DAPI. Negative controls were performed in which the primary antibody was substituted

460 with the same concentration of normal IgG of the appropriate isotype. Images were
461 obtained with a Zeiss LSM980 microscope.
462 Note that similar methods were used in (Sekulovski et al., 2023).
463
464 *Confocal microscopy of fixed samples*
465 Confocal Images of fixed samples were acquired using a Nikon-A1 (Nikon) and a Zeiss
466 LS980 laser scanning confocal microscopes. Non-3D images were generated using
467 Zen, FIJI (NIH) and Photoshop (Adobe).
468
469 *Immunostaining*
470 hPSC-amnion cysts grown on the coverslip were rinsed with PBS (Gibco) twice, fixed
471 with 4% paraformaldehyde (Sigma) for 60 min, then rinsed with PBS three times, and
472 permeabilized with 0.1% SDS (Sigma, in 1x PBS) solution for 60 min. The samples
473 were blocked in 4% heat-inactivated goat serum (Gibco) or 4% normal donkey serum
474 (Gibco) in PBS overnight at 4°C. The samples were incubated with primary antibody
475 solution prepared in blocking solution at 4°C for 48 hr, washed three times with PBS (30
476 min each), and incubated in blocking solution with goat or donkey raised Alexa Fluor-
477 conjugated secondary antibodies (Thermo Fisher), at room temperature for 24 hours.
478 Counter staining was performed using Hoechst 33342 (nucleus, Thermo Fisher
479 Scientific), Alexa-Fluor-conjugated wheat germ agglutinin (membrane, Thermo Fisher
480 Scientific) and Phalloidin (F-ACTIN, Thermo Fisher). All samples were mounted on
481 slides using 90% glycerol (in 1x PBS). When mounting hPSC-cysts samples, modeling
482 clay was used as a spacer between coverslip and slide to preserve lumenal cyst

483 morphology. Antibodies for IF staining are found in **Table 2**. Similar staining method
484 was previously used in (Shao et al., 2017a; Shao et al., 2017b).
485
486 *RNA isolation and Single cell RNA sequencing*
487 Gel-3D hPSC-amnion samples were rinsed once with cold 1x PBS prior to treating with
488 Cultrex Organoid Harvesting solution (R&D Systems) to non-enzymatically
489 depolymerize Ultimatrix (gel bed, R&D systems), which were then dissociated into
490 single cell suspensions using the Neural Tissue Dissociation Kit (P) (Miltenyi Biotech,
491 130-092-628) following the manufacturer's protocol with the exception that gentle
492 agitations were performed manually with a P1000 pipette and all incubations were
493 performed at 10°C. Cells were filtered through 70μm cell strainers (SP Bel-Art,
494 136800070), rinsed with ice cold 1x PBS and counted before proceeding with the 10x
495 Chromium Next Single Cell 3' v3.1 platform (single cell preparation, single cell isolation
496 and barcoding performed according to the manufacturer's instructions). Libraries were
497 sequenced (Illumina NovaSeq 6000 S4 flowcell, the DNA services laboratory of the Roy
498 J. Carver Biotechnology Center at the University of Illinois at Urbana-Champaign)
499 followed by quality control (adaptor trimming, de-duplication), alignment and
500 demultiplexing based on manufactured indices using Partek Flow software (Partek Inc.
501 St. Louis, MO, USA, CellRanger).
502
503 *Bioinformatics – single cell RNA sequencing dataset analysis*
504 Analysis of the d1-4 time-course amnion scRNA-seq dataset was performed using the
505 Seurat R package (v.4.2.1, (Hao et al., 2021)). For quality control, cells were filtered out

506 if the total number of detected genes was less than 1,500, if the expression percentage
507 from mitochondrial genes was less than 3% or greater than 15%, or if the total number
508 of transcripts was greater than 30,000. Expression values were then log-normalized
509 with scaling factor 10,000 for cell-level normalization, and further centered and scaled
510 across genes. Principal component analysis (PCA) was performed prior to embedding
511 8,765 cells into two-dimensional space with UMAP using top 15 PCs. Cell clusters were
512 identified using FindNeighbors and FindClusters functions based on a shared nearest
513 neighbor modularity optimization clustering algorithm (resolution set as 0.2). In addition,
514 the "early progenitor" cluster was identified within the original "progenitor" cluster
515 (containing both early and later progenitors) by a gating strategy that sets a cut-off
516 based on the normalized expression levels of TBXT (more than 0.4) and CLDN10 (less
517 than 3.8). Nearby $TBXT^-$ cells within the $TBXT^+$ domain were also included in the "early
518 progenitor" cluster using CellSelector function because those cells are likely due to
519 dropouts. The cluster marker genes were identified using FindAllMarkers function
520 (Wilcoxon Rank Sum test) with adjusted p values less than 0.05.
521
522 *Mapping and gene expression analyses of Tyser et al. Carnegie Stage 7 human embryo*
523 *single cell RNA sequencing dataset*
524 The original UMAP coordinates and annotations for all 1,195 cells were used in **Fig.**
525 **S1C** as well as in the accompanying expression plots. The processed data were
526 downloaded from http://www.human-gastrula.net, which was used to generate a UMAP
527 plot (using DimPlot function in R package Seurat), as well as to perform expression
528 analyses (FeaturePlot function in Seurat).

Integration and gene expression analyses of the d1-4 amnion and Tyser et al. Carnegie Stage 7 human embryo single cell RNA sequencing datasets

The two single cell datasets were integrated using a canonical correlation analysis based approach implemented in the IntegrateData function with 4,000 anchor features and 50 dimensions for anchor weighting in Seurat R package (v4.2.1).

Integration and gene expression analyses of Yang et al. GD14 cynomolgus macaque embryo single cell RNA sequencing dataset

The processed data were downloaded from GSE148683, and the ensemble genome build Macaca_fascicularis_5.0 release 96 was used to identify human orthogonal gene symbols. Datasets from two distinct GD14 embryos (Yang et al., 2021) were integrated using 5,000 anchor features and 10 dimensions in the IntegrateData function in Seurat R package (v.4.2.1) package: trophoblast cells were removed from the dataset prior to integration. Six general cell populations (epiblast, transition, mesoderm, amnion, endoderm and extraembryonic mesenchyme) were identified using FindClusters function (resolution as 0.4).

RNA velocity (scvelo) analysis

From the aligned BAM files, a loom file was generated for each d1-d4 dataset respectively using the function run10x mode in software velocyto (v0.17) with default parameters to create count matrices made of spliced and unspliced read counts (with Human genome annotation hg19). scVelo (Python package v.0.2.5 (Bergen et al., 2020)

552 was then used to analyze the loom files and examine RNA velocity. Inferred RNA
553 velocity was overlaid onto the UMAP embedding (created by Seurat pipeline as
554 described above) and visualized by stream plot (with default parameters except
555 smoothness was set to 1).
556

557 **FIGURES AND FIGURE LEGENDS**

558 **Figure 1. Single-cell transcriptomic signatures of developing Gel-3D human**
559 **amnion model**

560 (A) Confocal images of d1, d2, d3 and d4 hPSC-amnion cysts stained for TFAP2A, an
561 amnion marker, NANOG, a pluripotency marker, as well as for DNA (blue) and
562 membrane (magenta, using wheat germ agglutinin). White arrowheads indicate cells
563 that display weak TFAP2A expression. Scale bars = 20μm.
564 (B) Quantitation for nuclear aspect ratio, a measure of epithelial cell morphology, of
565 developing hPSC-amnion at indicated timepoints, revealing a gradual squamous
566 morphogenesis (quantitation method in **Fig. S1A**). * indicates $p < 0.05$.
567 (C,D) A UMAP plot displaying the single cell transcriptomes of 1,359 d1 (salmon), 1,546
568 d2 (sage), 2,352 d3 (light blue) and 3,508 d4 Gel-3D cells (C) with seven identified cell
569 populations (D, pluripotency-exiting (salmon, 1,363 cells), early progenitor (brown, 479
570 cells), late progenitor (sage, 1,045 cells), specified (green, 1,366 cells) and maturing
571 (purple, 2,795 cells), PGC-LC (primordial germ cell-like cells, blue, 1,055 cells) and CM-
572 LC (cardiac mesoderm-like cells, magenta, 662)).

573 (E-G) Expression of known early (E, *ID2*, *GATA3*, *TFAP2A*), specified (F, *ISL1*, *HAND1*,
574 *DLX5*) and late (G, *GABRP*, *VTCN1*, *IGFBP3*) amnion markers superimposed onto the
575 UMAP plot.
576 (H) RNA velocity analysis of the time-course Gel-3D dataset, showing predicted lineage
577 progression trajectories.
578 (I-K) A UMAP plot showing the integrated single cell transcriptomes of d1-d4 Gel-3D
579 and Tyser *et al.* CS7 embryo datasets, revealing close overlap of Gel-3D amnion
580 progressing cells with Tyser Epiblast, Primitive Streak and Ectoderm/Amnion cells
581 (shown in (I) with original sample, (J) with Gel-3D, and (K) with Tyser *et al.* annotations
582 (individual Tyser annotations plotted in **Fig. S1F**)).
583 (L,M) Expression of primordial germ cell (L, *PRDM1*, *SOX17*, *NANOS3*) and cardiac
584 mesoderm (M, *HAND2*, *GATA4*, *PITX2*) markers.
585 (N) Summary of marker expression.
586
587 **Figure 2. Transient expression of TBXT and CLDN10 marks amnion progenitor**
588 **populations**
589 (A,B) Expression of *TBXT* (A) and *CLDN10* (B) superimposed onto the time-course Gel-
590 3D UMAP plot.
591 (C) Expression summary of top three most differentially expressed genes in early
592 progenitor and late progenitor populations.
593 (D,E) Confocal micrographs of developing hPSC-amnion harvested at indicated
594 timepoints, stained with indicated markers. (D) Weak TBXT expression is present at d2
595 (white arrowheads), but is diminished by d3. (E) A white arrowhead indicates a

596 CLDN10/TFAP2A double-positive cell. CLDN10 expression is extinguished by d4.
597 Membrane was stained using wheat germ agglutinin. Scale bars = 20μm
598 (F) Quantitation of CLDN10 expressing cells per cyst in Gel-3D overtime (n = 25 cysts
599 per timepoint).
600
601 **Figure 3. CLDN10 is expressed in amnion progenitor cells at the amnion-epiblast**
602 **boundary of the PASE model as well as cynomolgus macaque peri-gastrula**
603 (A) Optical sections of PASE stained with indicated markers. White arrowheads indicate
604 CLDN10 staining at the amnion-epiblast boundary. Weak CLDN10 signal in the
605 pluripotent territory is likely due to weak CLDN10 expression in the pluripotent cells;
606 brighter signal in the pluripotent territory is likely caused by the boundary cell
607 extensions.
608 (B) Confocal images of a cynomolgus macaque embryo staged at CS6/7 stained using
609 indicated markers. CLDN10 is expressed at the transitioning boundary cells between
610 the amnion and the epiblast. Insets indicate magnified regions.
611 (C,D) Confocal images of cynomolgus macaque embryos staged at CS10 stained using
612 indicated markers. Insets indicate magnified regions. In the CS10 embryo (early
613 organogenesis stage), while some posterior boundary CLDN10 staining is seen (seen in
614 (iii)), the anterior CLDN10 staining is highly prominent at the amnion-anterior surface
615 ectoderm border (in (i)). CLDN10 is also enriched in the dorsal foregut labeled by ISL1/2
616 and SOX2 but not SOX17 (indicated by * in (ii)). **Fig. S3F** provides a bird's-eye view of
617 the CS10 embryo. HT, heat tube; FB, forebrain; YS, yolk sac. White arrowheads
618 indicate the foregut pocket, while white arrows indicate the hindgut pocket.

619 Scale bars = 20μm (A), 200μm (B), 500μm (C,D).

620

621 **Figure 4. CLDN10 is critical for maintaining amnion fate progression in the**

622 **progenitor population.**

623 (A-D) Confocal images of control (A,C) and *CLDN10*-KO (B,D) hPSC grown in Gel-3D,

624 harvested at indicated timepoints and stained with indicated markers. CLDN10

625 expression is not seen in the KO (B). In the absence of *CLDN10*, PGC-LC formation is

626 seen early in d2 cysts, and cyst organization is disrupted by d4. Scale bars = 50μm.

627 (E) Flow chart outlining five continuous amniogenic lineage progressing states with

628 representative markers.

629 (F) A schematic representation of primate peri-gastrula near the primitive streak

630 (generated based on images in **Fig. 3B**, purple cells indicate primitive streak-derived

631 disseminating cells). Transcriptional signatures consistent with amniotic lineage

632 progression (indicated by dotted arrow) are observed at the amnion-epiblast boundary:

633 progressing from $SOX2^+$ epiblast cells (blue), $CLDN10^+$ transitioning boundary cells

634 (green), and, then, to $ISL1^+$ lineage specified amnion (orange).

635

636 **Figure S1. Related to Figure 1**

637 (A) Confocal images of hPSC-amnion stained with indicated markers, outlining nuclear

638 aspect ratio quantitation.

639 (B) Expression of pluripotency markers, SOX2, NANOG and POU5F1, superimposed

640 onto the Gel-3D UMAP plot.

641 (C) A UMAP plot displaying the original single cell transcriptome coordinates of the CS7
642 human embryo described in Tyser *et al.*, shown with the original annotations.
643 (D,E) Expression of indicated broad (D) and late (E) amnion markers superimposed
644 onto the Tyser UMAP plot.
645 (F) UMAP plots showing the integrated single cell transcriptomes of d1-d4 Gel-3D and
646 Tyser *et al.* CS7 embryo datasets with individual Tyser annotations.
647
648 **Figure S2. Validation of selected specified and maturing markers in a cynomolgus**
649 **macaque embryo staged between CS12 and CS13**
650 (A,B) CS12/13 cynomolgus macaque embryo sections were stained for indicated
651 markers (A: *GABRP* – green, *SESN3* – red, *ISL1* – magenta; B: *ADAMTS18* – green,
652 *SESN3* – red, *ISL1* – magenta) using RNA *in situ* hybridization. (i) – (vii) indicate insets:
653 individual channels are shown in gray scale to aid visualization (from left to right:
654 *GABRP*, *SESN3*, *ISL1* and merge in (A), *ADAMTS18*, *SESN3*, *ISL1* in (B)), and dotted
655 lines indicate a layer of amniotic epithelium and mesenchyme. Most amnion cells are
656 positive for *GABRP*, *SESN3* and *ISL1*. *ADAMTS18* expression is restricted to a fraction
657 of cells. In (iv), there are four *ADAMTS18*^{high} cells, while *ADAMTS18* is largely
658 undetected in the amnion in (v). In (vi) and (vii), most cells are *ADAMTS18*^{high}.
659 FB; forebrain, HB, hindbrain; FG, foregut; C; cardiac tissue; NT, neural tube; S, somite.
660 * indicates an *ISL1*$^{+}$ tissue that is likely of genital tubercle lineage. Scale bars = 500μm.
661 (C) An overview image of the CS12/13 embryo implantation site shown in (A). Only
662 nuclear staining is shown in grayscale. Scale bar = 2mm.
663

664 **Figure S3. Additional expression analyses**

665 (A) Expression of *TBXT* and *CLDN10* superimposed onto the uncropped Tyser *et al.*
666 CS7 human embryo UMAP plot.

667 (B) A UMAP plot displaying the GD14 cynomolgus macaque single cell transcriptome
668 with six identified general clusters (epiblast – light blue; transition – purple; amnion –
669 gold; mesoderm – green; endoderm – teal; extraembryonic mesoderm – salmon). Arrow
670 indicates the likely trajectory of amnion differentiation based on the data in Yang *et al.*
671 as well as the expression analysis in (C). Note that, although not identical to the
672 published UMAP plot in Yang *et al.*, general characteristics are well recapitulated.
673 Trophectoderm cells have been omitted as performed in Yang *et al.*.

674 (C) Expression of indicated markers superimposed onto the Yang *et al.* UMAP plot. Late
675 amnion markers (EPAS1 and GABRP) are expressed at the tip of the TFAP2A and ISL1
676 double-positive amnion cluster. CLDN10 positive cells show a weak TBXT expression
677 level.

678 (D,E) Individual channels of the whole embryo images in **Fig. 3C** and **3D**, respectively.

679 (F) An overview image of the CS10 (**Fig. 3C**) embryo implantation sites (DNA signal
680 shown in gray scale, Scale bar = 2mm).

681

682 **Figure S4. Validation of two distinct *CLDN10*-KO hPSC lines**

683 (A) Sequenced genotyping results of *CLDN10*-KO #1 and #2 lines. KO lines #1 and #2
684 have similar phenotype, both displaying an increased formation of PGC-LC and
685 defective cyst organization. The second coding sequence of *CLDN10* was targeted.

686 (B) Representative sequence traces for each mutations.

687

688 **Table 1. Lists of differentially expressed genes in pluripotency-exiting (1506),**
689 **early progenitor (692), late progenitor (697), specified (944), maturing (868), PGC-**
690 **LC (1181) and CM-LC (746) clusters**

691

692 **Table 2. List of antibodies, RNAscope probes, primers and plasmids used in this**
693 **study**

694

695 **ACKNOWLEDGEMENTS**

696 We thank the Wisconsin National Primate Research Center (WNPRC) Veterinary,
697 Scientific Protocol Implementation, Pathology and Animal Services staff for providing
698 animal care, and assisting in procedures including breeding, pregnancy monitoring, and
699 sample collection. A special thanks to Michele Schotzko, Sara Shaw and Drs. Heather
700 Simmons and Puja Basu for their help in generating the macaque specimens. The
701 contents of this manuscript are solely the responsibility of the authors and do not
702 represent the official views of the NIH. We thank Dr. Deborah Gumucio for insightful
703 comments to the manuscript, as well as the Roy J. Carver Biotechnology Center at the
704 University of Illinois at Urbana-Champaign for sequence services.

705

706 **Funding:** This work was supported by NIH grants R01-HD098231 (K.T.), P51
707 OD011106 (to the WNPRC) as well as by MCW CBNA Start-up funds, Advancing a
708 Healthier Wisconsin (AHW) Endowment (16003-5520766, N.S.) and the Lalor
709 Foundation Postdoctoral Fellowship (N.S.). Specifically, MCW CBNA Start-up funds

710 were used to perform experiments using PASE. **Competing interests:** The authors
711 declare no competing interest. **Data and materials availability**: All data needed to
712 evaluate the conclusions in the paper are present in the paper and the Supplementary
713 Materials. The raw data, unfiltered count matrix and processed count matrix will be
714 available to the database of Genotypes and Phenotypes (dbGaP) upon publication.
715 Further information and requests for reagents may be directed to Kenichiro Taniguchi.
716

717 **REFERENCES**

718 Angelow, S., Ahlstrom, R., and Yu, A.S. (2008). Biology of claudins. Am J Physiol Renal
719 Physiol *295*, F867-876.
720 Bergen, V., Lange, M., Peidli, S., Wolf, F.A., and Theis, F.J. (2020). Generalizing RNA velocity
721 to transient cell states through dynamical modeling. Nature biotechnology *38*, 1408-1414.
722 Bergmann, S., Penfold, C.A., Slatery, E., Siriwardena, D., Drummer, C., Clark, S., Strawbridge,
723 S.E., Kishimoto, K., Vickers, A., Tewary, M.*, et al.* (2022). Spatial profiling of early primate
724 gastrulation in utero. Nature *609*, 136-143.
725 Butler, A., Hoffman, P., Smibert, P., Papalexi, E., and Satija, R. (2018). Integrating single-cell
726 transcriptomic data across different conditions, technologies, and species. Nature
727 biotechnology *36*, 411-420.
728 Carleton, A.E., Duncan, M.C., and Taniguchi, K. (2022). Human epiblast lumenogenesis:
729 From a cell aggregate to a lumenal cyst. Seminars in cell & developmental biology *131*, 117-
730 123.
731 Castillo-Venzor, A., Penfold, C.A., Morgan, M.D., Tang, W.W., Kobayashi, T., Wong, F.C.,
732 Bergmann, S., Slatery, E., Boroviak, T.E., Marioni, J.C.*, et al.* (2023). Origin and segregation of
733 the human germline. Life Sci Alliance *6*.
734 Chambers, S.M., Fasano, C.A., Papapetrou, E.P., Tomishima, M., Sadelain, M., and Studer, L.
735 (2009). Highly efficient neural conversion of human ES and iPS cells by dual inhibition of
736 SMAD signaling. Nature biotechnology *27*, 275-280.
737 Chen, D., Sun, N., Hou, L., Kim, R., Faith, J., Aslanyan, M., Tao, Y., Zheng, Y., Fu, J., Liu, W.*, et al.*
738 (2019). Human Primordial Germ Cells Are Specified from Lineage-Primed Progenitors. Cell
739 reports *29*, 4568-4582 e4565.
740 Chen, F., and LoTurco, J. (2012). A method for stable transgenesis of radial glia lineage in
741 rat neocortex by piggyBac mediated transposition. Journal of neuroscience methods *207*,
742 172-180.
743 Chen, K., Zheng, Y., Xue, X., Liu, Y., Resto Irizarry, A.M., Tang, H., and Fu, J. (2021). Branching
744 development of early post-implantation human embryonic-like tissues in 3D stem cell
745 culture. Biomaterials *275*, 120898.
746 Enders, A.C., Hendrickx, A.G., and Schlafke, S. (1983). Implantation in the rhesus monkey:
747 initial penetration of endometrium. The American journal of anatomy *167*, 275-298.

748 Enders, A.C., Schlafke, S., and Hendrickx, A.G. (1986). Differentiation of the embryonic disc,
749 amnion, and yolk sac in the rhesus monkey. The American journal of anatomy *177*, 161-
750 185.
751 Hamed, M.M., Taniguchi, K., and Duncan, M.C. (2023). Monitoring Effects of Membrane
752 Traffic Via Changes in Cell Polarity and Morphogenesis in Three-Dimensional Human
753 Pluripotent Stem Cell Cysts. Methods in molecular biology *2557*, 83-98.
754 Hao, Y., Hao, S., Andersen-Nissen, E., Mauck, W.M., 3rd, Zheng, S., Butler, A., Lee, M.J., Wilk,
755 A.J., Darby, C., Zager, M.*, et al.* (2021). Integrated analysis of multimodal single-cell data. Cell
756 *184*, 3573-3587 e3529.
757 Heemskerk, I., Burt, K., Miller, M., Chhabra, S., Guerra, M.C., and Warmflash, A. (2017).
758 Morphogen dynamics control patterning in a stem cell model of human embryo. bioRxiv
759 http://dx.doi.org/10.1101/202366.
760 Joy, D.A., Libby, A.R.G., and McDevitt, T.C. (2021). Deep neural net tracking of human
761 pluripotent stem cells reveals intrinsic behaviors directing morphogenesis. Stem cell
762 reports *16*, 1317-1330.
763 Lacoste, A., Berenshteyn, F., and Brivanlou, A.H. (2009). An efficient and reversible
764 transposable system for gene delivery and lineage-specific differentiation in human
765 embryonic stem cells. Cell stem cell *5*, 332-342.
766 Miki, T., Lehmann, T., Cai, H., Stolz, D.B., and Strom, S.C. (2005). Stem cell characteristics of
767 amniotic epithelial cells. Stem cells *23*, 1549-1559.
768 Minn, K.T., Fu, Y.C., He, S., Dietmann, S., George, S.C., Anastasio, M.A., Morris, S.A., and
769 Solnica-Krezel, L. (2020). High-resolution transcriptional and morphogenetic profiling of
770 cells from micropatterned human ESC gastruloid cultures. eLife *9*.
771 Nakamura, T., Okamoto, I., Sasaki, K., Yabuta, Y., Iwatani, C., Tsuchiya, H., Seita, Y.,
772 Nakamura, S., Yamamoto, T., and Saitou, M. (2016). A developmental coordinate of
773 pluripotency among mice, monkeys and humans. Nature *537*, 57-62.
774 Nakamura, T., Yabuta, Y., Okamoto, I., Sasaki, K., Iwatani, C., Tsuchiya, H., and Saitou, M.
775 (2017). Single-cell transcriptome of early embryos and cultured embryonic stem cells of
776 cynomolgus monkeys. Scientific data *4*, 170067.
777 Overeem, A.W., Chang, Y.W., Moustakas, I., Roelse, C.M., Hillenius, S., Helm, T.V., Schrier,
778 V.F.V., Goncalves, M., Mei, H., Freund, C.*, et al.* (2023). Efficient and scalable generation of
779 primordial germ cells in 2D culture using basement membrane extract overlay. Cell Rep
780 Methods *3*, 100488.
781 Pedroza, M., Gassaloglu, S.I., Dias, N., Zhong, L., Hou, T.J., Kretzmer, H., Smith, Z.D., and
782 Sozen, B. (2023). Self-patterning of human stem cells into post-implantation lineages.
783 Nature *622*, 574-583.
784 Perea-Gomez, A., Vella, F.D., Shawlot, W., Oulad-Abdelghani, M., Chazaud, C., Meno, C.,
785 Pfister, V., Chen, L., Robertson, E., Hamada, H.*, et al.* (2002). Nodal antagonists in the
786 anterior visceral endoderm prevent the formation of multiple primitive streaks.
787 Developmental cell *3*, 745-756.
788 Roost, M.S., van Iperen, L., Ariyurek, Y., Buermans, H.P., Arindrarto, W., Devalla, H.D.,
789 Passier, R., Mummery, C.L., Carlotti, F., de Koning, E.J.*, et al.* (2015). KeyGenes, a Tool to
790 Probe Tissue Differentiation Using a Human Fetal Transcriptional Atlas. Stem cell reports *4*,
791 1112-1124.
792 Rostovskaya, M., Andrews, S., Reik, W., and Rugg-Gunn, P.J. (2022). Amniogenesis occurs in
793 two independent waves in primates. Cell stem cell *29*, 744-759 e746.

794 Sasaki, K., Nakamura, T., Okamoto, I., Yabuta, Y., Iwatani, C., Tsuchiya, H., Seita, Y.,
795 Nakamura, S., Shiraki, N., Takakuwa, T.*, et al.* (2016). The Germ Cell Fate of Cynomolgus
796 Monkeys Is Specified in the Nascent Amnion. Developmental cell *39*, 169-185.
797 Schultheiss, T.M., Burch, J.B., and Lassar, A.B. (1997). A role for bone morphogenetic
798 proteins in the induction of cardiac myogenesis. Genes & development *11*, 451-462.
799 Sekulovski, N., Wettstein, J.C., Carleton, A.E., Taniguchi, L.E., Ma, X., Rao, S., Schmidt, J.K.,
800 Golos, T.G., Lin, C.-W., and Taniguchi, K. (2023). Temporally resolved early BMP-driven
801 transcriptional cascade during human amnion specification. eLife *12: RP89367*.
802 Shahbazi, M.N., and Zernicka-Goetz, M. (2018). Deconstructing and reconstructing the
803 mouse and human early embryo. Nature cell biology.
804 Shao, Y., and Fu, J. (2022). Engineering multiscale structural orders for high-fidelity
805 embryoids and organoids. Cell stem cell *29*, 722-743.
806 Shao, Y., Taniguchi, K., Gurdziel, K., Townshend, R.F., Xue, X., Yong, K.M.A., Sang, J., Spence,
807 J.R., Gumucio, D.L., and Fu, J. (2017a). Self-organized amniogenesis by human pluripotent
808 stem cells in a biomimetic implantation-like niche. Nature materials *16*, 419-425.
809 Shao, Y., Taniguchi, K., Townshend, R.F., Miki, T., Gumucio, D.L., and Fu, J. (2017b). A
810 pluripotent stem cell-based model for post-implantation human amniotic sac development.
811 Nature communications *8*, 208.
812 Shawlot, W., Wakamiya, M., Kwan, K.M., Kania, A., Jessell, T.M., and Behringer, R.R. (1999).
813 Lim1 is required in both primitive streak-derived tissues and visceral endoderm for head
814 formation in the mouse. Development *126*, 4925-4932.
815 Taniguchi, K., Heemskerk, I., and Gumucio, D.L. (2019). Opening the black box: Stem cell-
816 based modeling of human post-implantation development. The Journal of cell biology *218*,
817 410-421.
818 Taniguchi, K., Shao, Y., Townshend, R.F., Tsai, Y.H., DeLong, C.J., Lopez, S.A., Gayen, S.,
819 Freddo, A.M., Chue, D.J., Thomas, D.J.*, et al.* (2015). Lumen Formation Is an Intrinsic
820 Property of Isolated Human Pluripotent Stem Cells. Stem cell reports *5*, 954-962.
821 Townshend, R.F., Shao, Y., Wang, S., Cortez, C.L., Esfahani, S.N., Spence, J.R., O'Shea, K.S., Fu,
822 J., Gumucio, D.L., and Taniguchi, K. (2020). Effect of Cell Spreading on Rosette Formation by
823 Human Pluripotent Stem Cell-Derived Neural Progenitor Cells. Front Cell Dev Biol *8*,
824 588941.
825 Tsaytler, P., Liu, J., Blaess, G., Schifferl, D., Veenvliet, J.V., Wittler, L., Timmermann, B.,
826 Herrmann, B.G., and Koch, F. (2023). BMP4 triggers regulatory circuits specifying the
827 cardiac mesoderm lineage. Development *150*.
828 Tyser, R.C.V., Mahammadov, E., Nakanoh, S., Vallier, L., Scialdone, A., and Srinivas, S. (2021).
829 Single-cell transcriptomic characterization of a gastrulating human embryo. Nature *600*,
830 285-289.
831 van Wijk, B., Moorman, A.F., and van den Hoff, M.J. (2007). Role of bone morphogenetic
832 proteins in cardiac differentiation. Cardiovasc Res *74*, 244-255.
833 Vasic, I., Libby, A.R.G., Maslan, A., Bulger, E.A., Zalazar, D., Krakora Compagno, M.Z., Streets,
834 A., Tomoda, K., Yamanaka, S., and McDevitt, T.C. (2023). Loss of TJP1 disrupts gastrulation
835 patterning and increases differentiation toward the germ cell lineage in human pluripotent
836 stem cells. Developmental cell *58*, 1477-1488 e1475.
837 Wang, S., Lin, C.W., Carleton, A.E., Cortez, C.L., Johnson, C., Taniguchi, L.E., Sekulovski, N.,
838 Townshend, R.F., Basrur, V., Nesvizhskii, A.I.*, et al.* (2021). Spatially resolved cell polarity
839 proteomics of a human epiblast model. Sci Adv *7*.

840 Warmflash, A., Sorre, B., Etoc, F., Siggia, E.D., and Brivanlou, A.H. (2014). A method to
841 recapitulate early embryonic spatial patterning in human embryonic stem cells. Nature
842 methods *11*, 847-854.
843 Xiao, Z., Cui, L., Yuan, Y., He, N., Xie, X., Lin, S., Yang, X., Zhang, X., Shi, P., Wei, Z.*, et al.* (2024).
844 3D reconstruction of a gastrulating human embryo. Cell *187*, 2855-2874 e2819.
845 Yang, R., Goedel, A., Kang, Y., Si, C., Chu, C., Zheng, Y., Chen, Z., Gruber, P.J., Xiao, Y., Zhou, C.*,*
846 *et al.* (2021). Amnion signals are essential for mesoderm formation in primates. Nature
847 communications *12*, 5126.
848 Zhao, C., Plaza Reyes, A., Schell, J.P., Weltner, J., Ortega, N.M., Zheng, Y., Björklund, Å.K.,
849 Baque-Vidal, L., Sokka, J., Torokovic, R.*, et al.* (2024). A comprehensive human
850 embryogenesis reference tool using single-cell RNA sequencing data. bioRxiv *doi:*
851 *10.1101/2021.05.07.442980*.
852 Zheng, Y., Xue, X., Shao, Y., Wang, S., Esfahani, S.N., Li, Z., Muncie, J.M., Lakins, J.N., Weaver,
853 V.M., Gumucio, D.L.*, et al.* (2019). Controlled modelling of human epiblast and amnion
854 development using stem cells. Nature *573*, 421-425.
855 Zheng, Y., Yan, R.Z., Sun, S., Kobayashi, M., Xiang, L., Yang, R., Goedel, A., Kang, Y., Xue, X.,
856 Esfahani, S.N.*, et al.* (2022). Single-cell analysis of embryoids reveals lineage diversification
857 roadmaps of early human development. Cell stem cell *29*, 1402-1419 e1408.
858

Figure 1

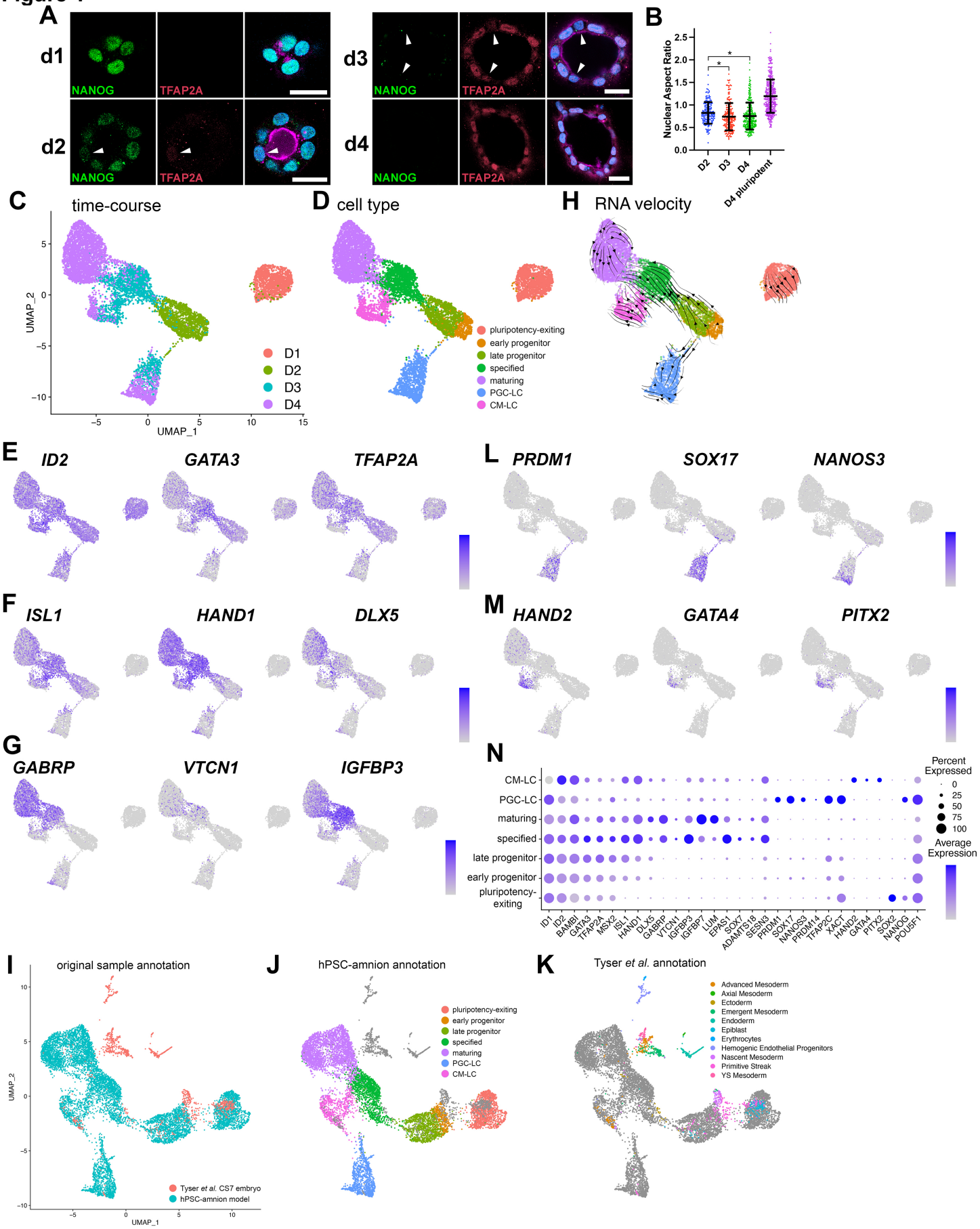
A
d1
d2
d3
d4
NANOG
TFAP2A
B
Nuclear Aspect Ratio
D2
D3
D4
D4 pluripotent
C
time-course
UMAP_1
UMAP_2
D1
D2
D3
D4
D
cell type
pluripotency-exiting
early progenitor
late progenitor
specified
maturing
PGC-LC
CM-LC
H
RNA velocity
E
ID2
GATA3
TFAP2A
L
PRDM1
SOX17
NANOS3
F
ISL1
HAND1
DLX5
M
HAND2
GATA4
PITX2
G
GABRP
VTCN1
IGFBP3
N
CM-LC
PGC-LC
maturing
specified
late progenitor
early progenitor
pluripotency-exiting
Percent Expressed
Average Expression
I
original sample annotation
Tyser et al. CS7 embryo
hPSC-amnion model
J
hPSC-amnion annotation
K
Tyser et al. annotation
Advanced Mesoderm
Axial Mesoderm
Ectoderm
Emergent Mesoderm
Endoderm
Epiblast
Erythrocytes
Hemogenic Endothelial Progenitors
Nascent Mesoderm
Primitive Streak
YS Mesoderm

Figure 2

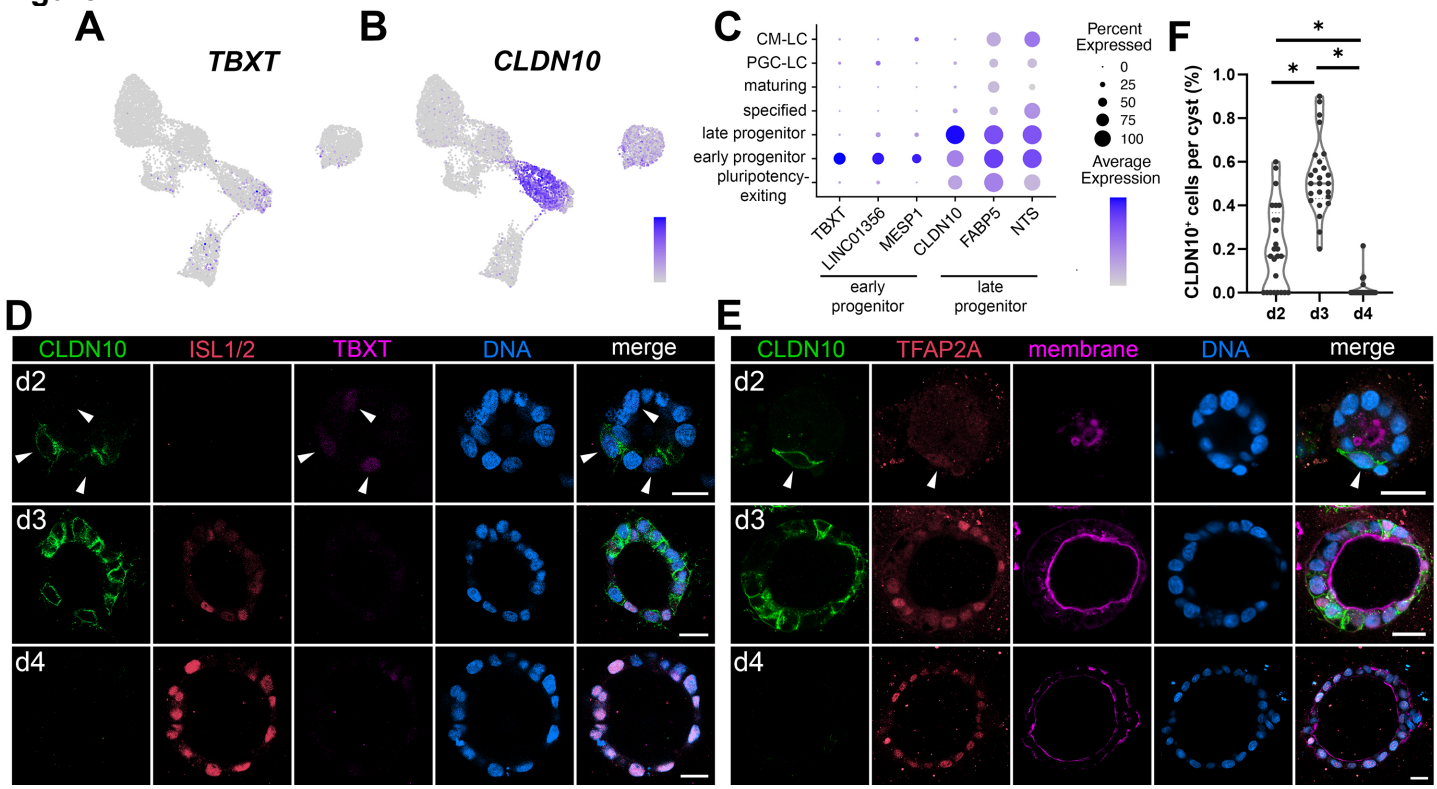
A
TBXT
B
CLDN10
C
CM-LC
PGC-LC
maturing
specified
late progenitor
early progenitor
pluripotency-exiting
TBXT
LINC01356
MESP1
CLDN10
FABP5
NTS
early progenitor
late progenitor
Percent Expressed
0
25
50
75
100
Average Expression
F
CLDN10⁺ cells per cyst (%)
1.0
0.8
0.6
0.4
0.2
0.0
d2
d3
d4
*
*
*
D
CLDN10
ISL1/2
TBXT
DNA
merge
d2
d3
d4
E
CLDN10
TFAP2A
membrane
DNA
merge
d2
d3
d4

Figure 3

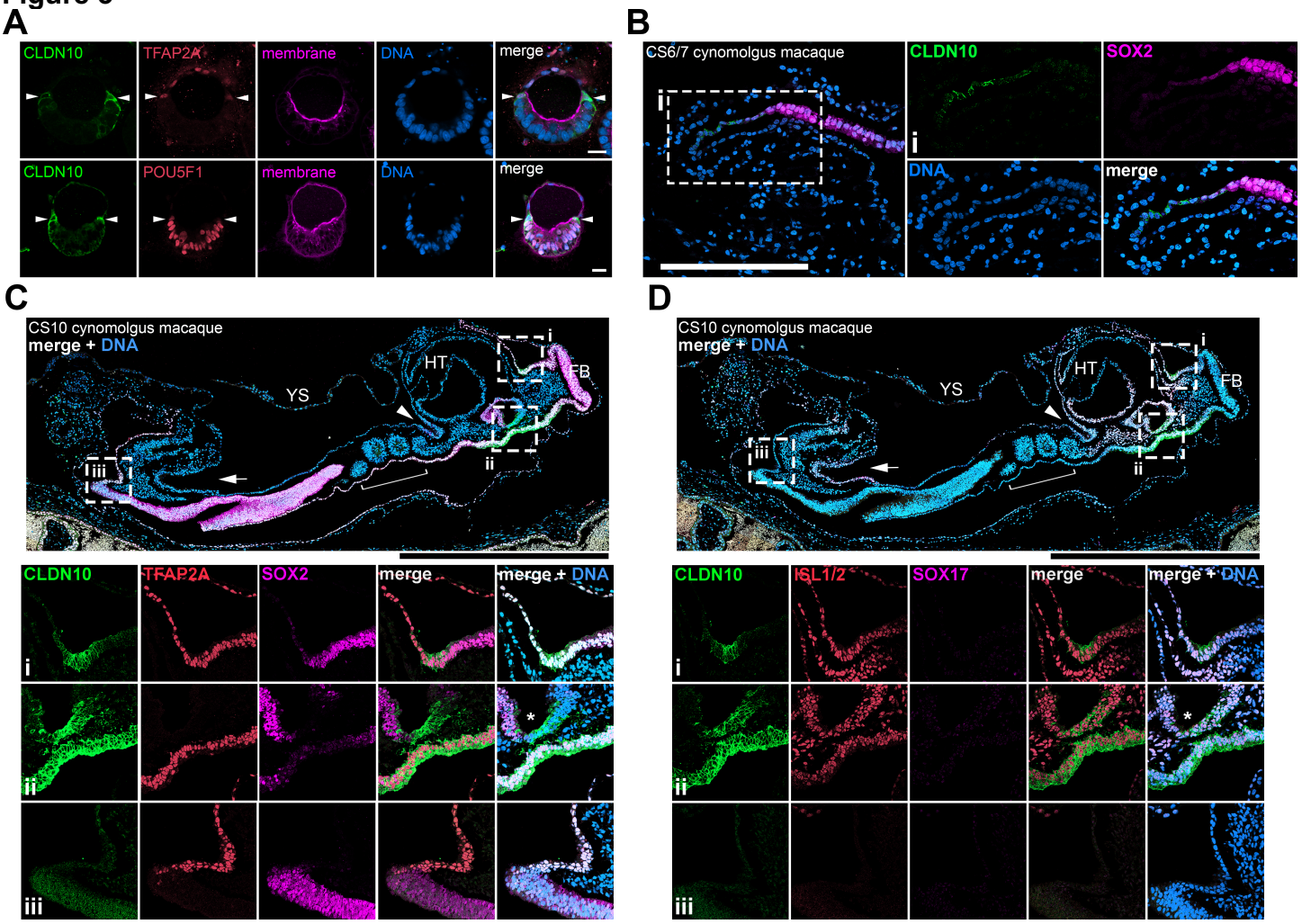
A
CLDN10
TFAP2A
membrane
DNA
merge
CLDN10
POU5F1
membrane
DNA
merge
B
CS6/7 cynomolgus macaque
CLDN10
SOX2
i
DNA
merge
C
CS10 cynomolgus macaque
merge + DNA
YS
HT
FB
i
ii
iii
CLDN10
TFAP2A
SOX2
merge
merge + DNA
*
D
CS10 cynomolgus macaque
merge + DNA
YS
HT
FB
i
ii
iii
CLDN10
ISL1/2
SOX17
merge
merge + DNA
*

Figure 4

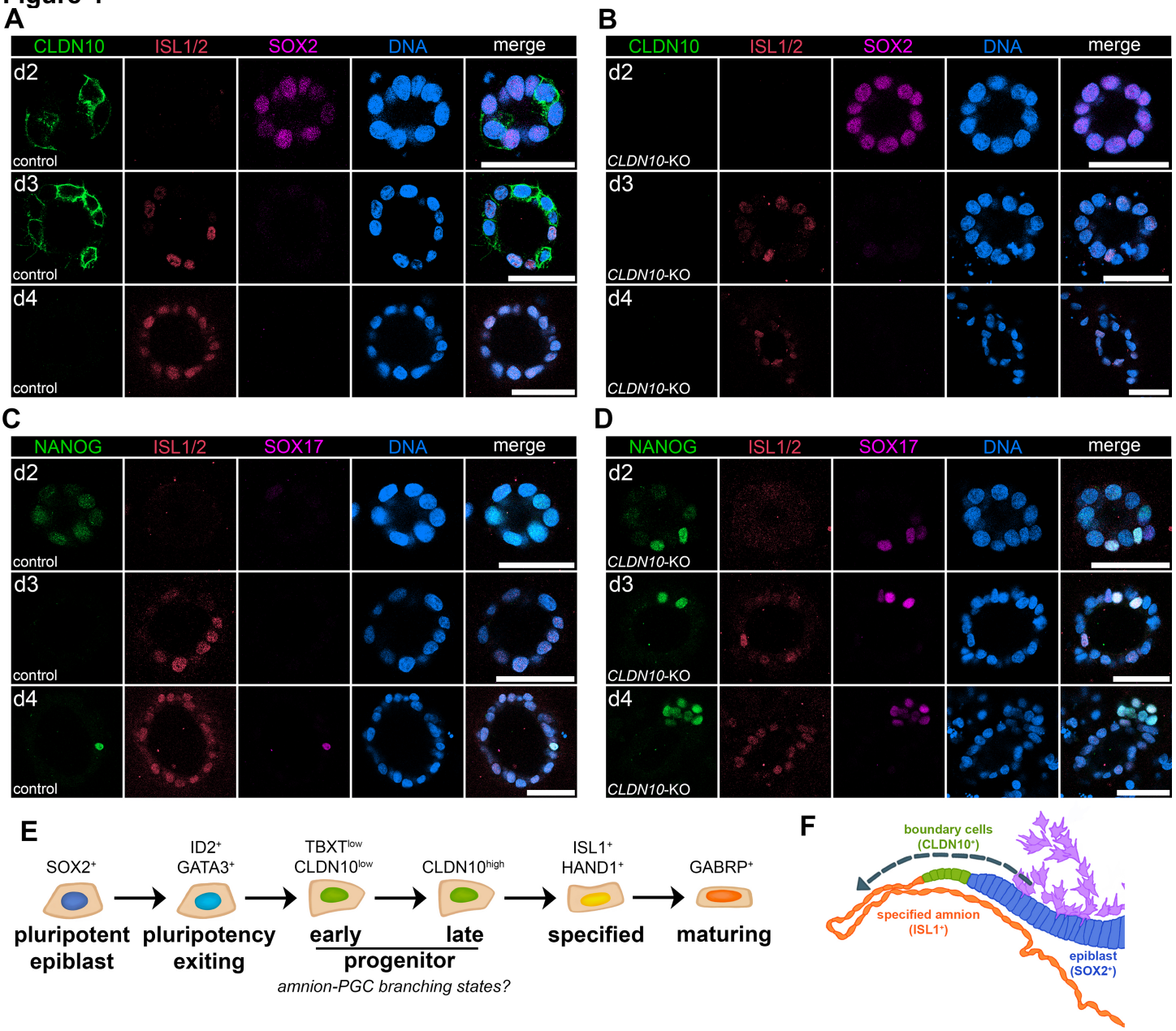
A
CLDN10
ISL1/2
SOX2
DNA
merge
d2
d3
d4
control
B
CLDN10-KO
C
NANOG
SOX17
D
E
SOX2+
pluripotent epiblast
ID2+
GATA3+
pluripotency exiting
TBXTlow
CLDN10low
early
CLDN10high
late
progenitor
ISL1+
HAND1+
specified
GABRP+
maturing
amnion-PGC branching states?
F
boundary cells (CLDN10+)
specified amnion (ISL1+)
epiblast (SOX2+)